

Numerical study of reflectance imaging using a parallel Monte Carlo method

Cheng Chen and Jun Q. Lu

Department of Physics, East Carolina University, Greenville, North Carolina 27858

Kai Li

Intel Corp., 2111 N.E. 25th Avenue, M/S JF3-336, Hillsboro, Oregon 97124

Suisheng Zhao

Cisco Systems, Inc., 170 West Tasman Dr., San Jose, California 95134

R. Scott Brock and Xin-Hua Hu^{a)}

Department of Physics, East Carolina University, Greenville, North Carolina 27858

(Received 5 January 2007; revised 16 March 2007; accepted for publication 8 May 2007; published 22 June 2007)

Reflectance imaging of biological tissues with visible and near-infrared light has the significant potential to provide a noninvasive and safe imaging modality for diagnosis of dysplastic and malignant lesions in the superficial tissue layers. The difficulty in the extraction of optical and structural parameters lies in the lack of efficient methods for accurate modeling of light scattering in biological tissues of turbid nature. We present a parallel Monte Carlo method for accurate and efficient modeling of reflectance images from turbid tissue phantoms. A parallel Monte Carlo code has been developed with the message passing interface and evaluated on a computing cluster with 16 processing elements. The code was validated against the solutions of the radiative transfer equation on the bidirectional reflection and transmission functions. With this code we investigated numerically the dependence of reflectance image on the imaging system and phantom parameters. The contrasts of reflectance images were found to be nearly independent of the numerical aperture (NA) of the imaging camera despite the fact that reflectance depends on the NA. This enables efficient simulations of the reflectance images using an NA at 1.00. Using heterogeneous tissue phantoms with an embedded region simulating a lesion, we investigated the correlation between the reflectance image profile or contrast and the phantom parameters. It has been shown that the image contrast approaches 0 when the single-scattering albedos of the two regions in the heterogeneous phantoms become matched. Furthermore, a zone of detection has been demonstrated for determination of the thickness of the embedded region and optical parameters from the reflectance image profile and contrast. Therefore, the utility of the reflectance imaging method with visible and near-infrared light has been firmly established. We conclude from these results that the optical parameters of the embedded region can be determined inversely from reflectance images acquired with full-field illumination at multiple incident angles or multiple wavelengths. © 2007 American Association of Physicists in Medicine. [DOI: [10.1118/1.2745241](https://doi.org/10.1118/1.2745241)]

Key words: reflectance imaging, Monte Carlo simulation, optical imaging

I. INTRODUCTION

It has long been recognized that penetration of visible and near-infrared light into biological tissues such as the human skin renders us the ability to develop noninvasive methods for diagnosis of embedded lesions from the reflected light signals.¹⁻³ Therefore, quantitative determination of optical parameters of these embedded lesions from reflectance images is highly desirable for revealing pathological abnormalities as the optical imaging systems of large dynamic ranges and extended spectral sensitivity become readily available. Compared to the conventional imaging modalities such as x-ray computed tomography, magnetic-resonance imaging, and ultrasound imaging, the reflectance imaging method's benefits include safety with nonionizing radiation, high spatial resolution and low instrumentation costs. An existing barrier to achieve the above goal, however, relates to the lack

of accurate and fast modeling tools for quantitative understanding of reflectance image data from biological tissues of high turbidity. The strong and volumetric light scattering in most biological tissues causes the conventional methods of image reconstruction, such as the Radon transformation in conventional tomography, useless since the signals are assumed to propagate between sources and detectors along straight lines in these methods. In the spectral regions of the visible and near-infrared, signals consist mainly of the photons scattered away from the incident direction and the light scattering has to be accounted for accurately for tomographic reconstruction of optical parameters.

On the macroscopic scales of 0.1 mm or larger, it has been widely accepted that the radiative transfer theory provides a sufficiently accurate model to understand light transportation in turbid medium⁴ which can be further simplified

with diffusion approximations if multiple scattering dominates light distribution. Except for a few problems of simple geometry, closed-form solutions of boundary-value problems consisting of the radiative transfer equation (RTE) and the Fresnel's equations are not available. Other methods have been developed to model reflectance image data including diffusion approximations and the statistical sampling method of Monte Carlo (MC) simulations. The diffusion approximations have attracted intense interests because of their potential to yield closed-form solutions for rapid modeling of reflected light signals from a turbid medium.^{5,6} For heterogeneous tissue phantoms with embedded structures, numerical methods are still required to solve the diffusion equations.⁷ In either case of homogeneous or heterogeneous phantoms, diffusion approximations could lead to significant errors in calculating light distributions near interfaces of modest or large index mismatch and at small source-detector distances such as the case with full-field illumination and a large anisotropy factor of scattering.

By contrast, the method of MC simulations provides an accurate tool to solve boundary-value problems that do not have to have probabilistic contents, if the output variance is reduced sufficiently by adequate sampling. The simplicity of the MC algorithm enables rapid adaptation to problems with irregularly shaped structures and boundaries, including those of tissue optics based on the RTE and Fresnel equations.^{8–12} In addition, the MC algorithm yields robust performance in comparison with the direct solutions of RTE or diffusion equations, i.e., the performance of the MC algorithm does not depend on the detailed forms of the problems such as the temporal or spatial profiles of the excitation sources. The MC methods and variants such as the perturbation MC method have been used for forward calculations of signals to reconstruct optical or other system parameter distributions from the measured signals using gradient based inverse algorithm¹³ or simulated annealing algorithm.¹⁴

The obstacle to wide application of the MC method lies in the high computational cost for reducing the output variance. This drawback is particularly augmented in modeling of reflectance images of high spatial resolutions from heterogeneous tissue phantoms where variance reduction techniques, such as sampling size increase and correlated sampling,¹⁵ cannot be applied. Nevertheless, the rapid increase of performance-to-price ratio of computers over the last two decades has reduced this difficulty drastically. Consequently, it becomes possible now to develop an accurate and fast method of MC simulations for modeling imaging data by algorithm optimization and code parallelization.

MC methods have been recently applied to study the reflectance images from turbid media.^{16,17} As a prelude of our long-term research plan for developing MC based inverse algorithms to extract tissue optical parameters from image data, we present here a parallel MC method for rapid modeling of reflectance image data on a computing cluster. The parallel MC code has been validated and evaluated. We applied this code to investigate numerically the dependence of reflectance image data on the optical and structural parameters of heterogeneous tissue phantoms under the condition

of full-field illumination. The implications of these results on experimental and clinical studies are discussed.

II. MODELING METHODS

A. The Monte Carlo algorithm of photon tracking and counting

A MC method has been developed previously to calculate the light distribution in terms of a photon density within the framework of RTE and Fresnel's equations with the details published elsewhere.^{11,12} The light propagation in a tissue phantom is characterized by an absorption coefficient μ_a , a scattering coefficient μ_s , a single-scattering phase function $p(\mathbf{s}, \mathbf{s}')$ and a real refractive index n , where \mathbf{s}, \mathbf{s}' are unit vectors indicating the light propagation directions. A one-parameter function proposed by Henyey and Greenstein, $p(\cos \Theta)$, is used as the phase function in all simulations reported here with $\cos \Theta = \mathbf{s} \cdot \mathbf{s}'$.⁴ The function $p(\cos \Theta)$ is characterized by an anisotropy factor g defined as the first moment of $p(\cos \Theta)$, i.e., $g = \int_{4\pi} p(\cos \Theta) \cos \Theta d\Omega$. With $p(\cos \Theta)$ as the phase function, the optical properties of a turbid medium can be represented by a group of four scalar parameters as (μ_a, μ_s, g, n) or (μ_t, a, g, n) within the framework of RTE, where $\mu_t = \mu_a + \mu_s$ is the attenuation coefficient and $a = \mu_s / \mu_t$ is the single-scattering albedo. Different versions of our MC code built on the same kernel have been validated extensively.^{11,12,18–21} The relevant features of the current version for calculations of reflectance images are presented briefly here.

To simulate the light distribution reflected from a heterogeneous tissue phantom, different regions in the phantom are assigned with different sets of (μ_a, μ_s, g, n) . In this paper we focus our efforts on either a homogeneous phantom or a heterogeneous phantom in air with one embedded region of optical parameters different from its semi-infinite host. An incident light beam of uniform circular profile is represented by N_0 incident photons distributed uniformly over the illuminated region at the phantom surface. Of these photons, $N = N_0[1 - R_f(\theta_0)]$ photons enter the phantom at a refraction angle determined from the incident angle θ_0 by Snell's law and $R_f(\theta_0)$ is the unpolarized Fresnel reflection coefficient of the phantom surface.

Each photon entered into the phantom is tracked along its trajectory in the MC code. The coordinate system and book keeping scheme of the tracked photon's trajectory are adopted from those described in Refs 9 and 10. Different from the MC algorithm employed there, we first determine a life pathlength L_{ai} of the tracked photon in the i th region of $(\mu_{ai}, \mu_{si}, g_i, n_i)$ in the phantom by a random number (RN) according to an exponential distribution with a mean value, among all tracked photons, $\langle L_{ai} \rangle = 1 / \mu_{ai}$ before tracking starts.¹¹ The free path length $L_{si,\beta}$ of the photon before the next scattering event, i.e., the size of β th step with $\beta = 1, 2, 3, \dots$, is determined similarly by a RN with $\langle L_{si,\beta} \rangle = 1 / \mu_{si}$ while the direction of scattered photon is determined by two RNs mapped for the polar angle Θ according to the phase function $p(\cos \Theta)$ of parameter g and uniformly for the azimuth angle Φ . The tracking of the photon stops when

either it exits the turbid phantom or the accumulated path-length $\sum_{\beta} L_{si,\beta} > L_{ai}$. If a tracked photon is incident on an interface with another (j th) region of different optical parameters $(\mu_{aj}, \mu_{sj}, g_j, n_j)$, the unpolarized Fresnel reflectivity is calculated according to the incident angle and index mismatch, which is then used to determine if the photon reflects from or transmits through the interface by comparing to a RN.¹² If a photon travels inside the i th region over a path-length $l < L_{si,\gamma}$ before the γ th step is completed and enters into the j th region, its residual free path length $L_{si,\gamma} - l$ and residual life pathlength $L_{ai} - (l + \sum_{\beta=1}^{\gamma-1} L_{si,\beta})$ are respectively renormalized to produce $L_{sj,1}$ and L_{aj} as the updated first free path length and life path length in the j th region by

$$L_{sj,1} = \frac{n_i \mu_{si}}{n_j \mu_{sj}} (L_{si,\gamma} - l), \quad (1)$$

$$L_{aj} = \frac{n_i \mu_{ai}}{n_j \mu_{aj}} \left(L_{ai} - l - \sum_{\beta=1}^{\gamma-1} L_{si,\beta} \right). \quad (2)$$

The above renormalization scheme is established on the fact that RTE depends only on the path length $n\mu_s dL$ (see Ch. 3 of Refs. 22 and 23) and similar formulas have been previously used by others.¹⁰ The simulated reflectance images register only those exiting photons collected by the imaging system within the numerical aperture NA. After all photons entering into the phantom have been tracked, the density of the registered photons at the surface of the phantom is obtained as the output images.

The independent tracking of photons makes MC simulations ideal for parallel computing on a cluster with multiple processing elements (PEs). We employed a message passing interface (MPI) model for parallization of our sequential MC code, which includes the following steps. A MPI header file is included in the code to call subroutines from the MPI libraries for tasks such as initialization of MPI environment and passing messages among the PEs. A function is added in the photon tracking module to divide N tracked photons into groups for distribution among different PEs and another in the input/output module to collect tracking results from all PEs for the code output. In addition, two data files ("mpd.hosts" and "mpd.conf") are loaded at the cluster server, which are used by the startup script files to provide the IP addresses of the PEs used for parallel computing and login credentials.

The RNs used in the MC simulations need to be generated independently and uniformly between 0 and 1 for describing the random events of light scattering and absorption. Many RNs, 100 or more per tracked photon in most cases here, are required in a simulation and an appropriate random number generator (RNG) with a long sequence period is essential to ensure the accuracy of the simulation results. The random events in the photon tracking process can be sorted into different types according to the nature of the light-tissue interaction such as the scattering, absorption, and reflection from or refraction through an interface. To ensure the randomness for accurate MC modeling on the basis of ergodic hypothesis

it is necessary to assign each type of random events a unique sequence of RNs. This means that several independent RN sequences co-exist in a MC simulation.

A high-performance parallel code executed on a cluster of PEs requires minimization of data communication and PE idle time. It is thus preferable to have the RNs generated locally at each PE during photon tracking. The key in the parallization of our MC code is to develop a special RNG that can maintain the coexisting RN sequences on each PE with minimal correlations during a parallel computation. A good RNG for parallel computing should therefore yield results that are reproducible and independent of the PE numbers. To fulfill these requirements, we adapted a RNG by modifying an existing one (Ran4).²⁴ The original Ran4, based on a simple parameterization scheme,²⁵ accepts one integer argument as the seed and uses 32 bit operations on two 32 bit integers. It was first modified to extend to 64 bit integers to accommodate the requirement of long period in RN sequences in our case. Then an index number, as one of the two integers for the bit operations, was added to the argument to control the entry point of the sequence. These steps led to a new RNG (64 bit-Ran4) of two arguments consisting a seed and an index, where a uniqueness sequence is started by the seed and random or sequential access of a particular RN in a given sequence is governed by the index.¹⁶ We have tested the 64 bit-Ran4 extensively with an online test suite with results satisfying all statistical criteria for a high quality parallel RNG.²⁶ The new RNG has a very long sequence period and is also suitable for sequential calculations. At the start of a parallel MC simulation, a unique group of RNG seeds is passed to each PE and the PE establishes its own set of RN sequences through 64 bit-Ran4 for tracking the assigned package of photons.

B. Tissue phantoms and modeling of reflected light

In the simulation results reported here, we considered both homogeneous and heterogeneous tissue phantoms illuminated by an incident beam of diameter $2w$ at an incident angle of θ_0 , as shown in Fig. 1. For homogeneous slab phantoms of finite thickness T along the z axis, the optical parameters are given by $(\mu_{a1}, \mu_{s1}, g_1, n_1)$. To imitate embedded lesions in normal tissues,²⁷ we employed a heterogeneous tissue phantom with a region 2 of $(\mu_{a2}, \mu_{s2}, g_2, n_2)$ embedded in a semi-infinite host medium, the region 1, of $(\mu_{a1}, \mu_{s1}, g_1, n_1)$ with $T \rightarrow \infty$. For this study, we tested both cuboidal or cylindrical shapes for the embedded region 2 and found the results were identical in their main features. The cylindrical shape was adopted for region 2 with a diameter B in the x - y plane and a thickness D . The optical parameters of the heterogeneous phantoms were chosen mainly on the basis of our previously measured bulk values of the porcine and human skin tissues from 300 to 1600 nm in wavelength^{20,28} and those of melanin² and other pigments.²⁹ The parameter ranges of the two regions are listed in Table I.

The reflected light from a turbid phantom illuminated by an incident beam consists of two components, one due to the Fresnel or specular reflection at the interfaces between media

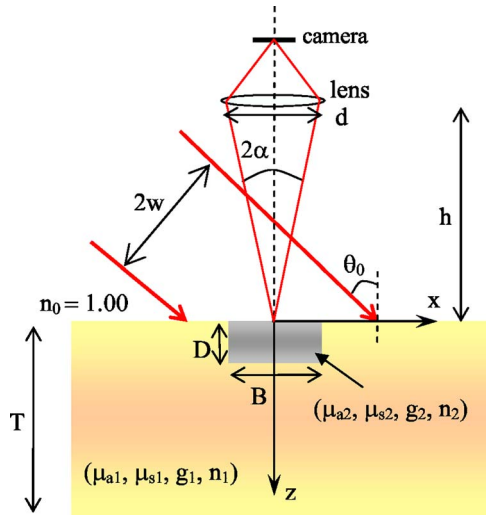


FIG. 1. The configuration of the incident light beam, turbid phantom, and optical system for acquisition of spatially resolved images. For semi-infinite heterogeneous phantoms $T \rightarrow \infty$ (in simulations, $T=100$ mm) while for homogeneous slab phantoms $D=B=0$.

of mismatched refractive indices³⁰ and another due to the remitted light from the bulk of the phantom. Even though the two components cannot be fully separated experimentally in all cases, they are distinctive in MC simulations. In all results presented in this paper, we intentionally removed the component of the specular reflection from the reflected light signals even for zero-lens-phantom distances ($h=0$ or $NA=1$) since it contains no quantitative information on the optical parameters of μ_a, μ_s, g of the phantom. Experimentally, this can be achieved by either an index-matching method³ or placing the detector away from the specularly reflected light for phantoms with optically smooth and flat surfaces.

The reflected light signals can be analyzed in forms of either spatially resolved distributions on a surface with angle-integrated signals or angle-resolved distributions. The former is natural, because human eyes and most cameras acquire such distributions as images, and can be applied to any type of phantoms while the latter is used in analysis of ideal cases of infinitely large homogeneous phantoms illuminated by a plane wave in which the reflected light distributes uniformly at the phantom surface.

For semi-infinite homogeneous slab phantoms with plane parallel surfaces, the response to a plane-wave beam of radiance L_{in} at the incident angles of (θ_0, ϕ_0) can be expressed in terms of a bidirectional reflection function R_b and a bidirectional transmission function T_b that yield, respectively, the outgoing radiances at exit angles of (θ, ϕ) as⁴

$$L_r(\mu, \phi) = \int_{2\pi} R_b(\mu, \phi; \mu_0, \phi_0) L_{in}(\mu_0, \phi_0) \frac{\mu_0}{\pi} d\Omega_0$$

$$= \int_0^1 R_b(\mu, \mu_0) L_{in}(\mu_0) 2\mu_0 d\mu_0 \quad (3)$$

for reflected light with $\mu = |\cos \theta|$, $\mu_0 = |\cos \theta_0|$ and $d\Omega_0 = d\mu_0 d\phi_0$, and

$$L_t(\mu, \phi) = \int_{2\pi} T_b(\mu, \phi; \mu_0, \phi_0) L_{in}(\mu_0, \phi_0) \frac{\mu_0}{\pi} d\Omega_0$$

$$= \int_0^1 T_b(\mu, \mu_0) L_{in}(\mu_0) 2\mu_0 d\mu_0 \quad (4)$$

for the transmitted light. It is easy to show with a unidirectional incident beam that the above definition of reflection function R_b leads to the conventional diffuse reflectance R_d for homogeneous media satisfying the Lambert cosine law. The functions R_b and T_b are used later in validation of our MC code with the homogeneous slab phantoms.

In MC simulations of spatially resolved reflected light distributions, or reflectance images, we first obtain the density distributions of remitted photons, $\rho(x, y, 0_-)$, at the air side of phantom surface of $z=0_-$ from the MC code with a 201×201 grid. Only those photons that can be collected through the aperture of the imaging lens are registered toward the aperture of the imaging lens to simulate the reflectance images by an ideal imaging lens with no aberrations and an numerical aperture $NA = \sin \alpha$ and a camera sensor aligned along the z axis to eliminate specularly reflected light from the air-phantom interface, as shown in Fig. 1. Without losing generality, we assume that the transmittance of the imaging lens remains 100% over the field of view (FOV) since only the relative distribution of photons in a reflectance image is concerned. From the output of the MC code, the reflectance image $R(x, y)$ is then calculated from the following

$$R(x, y) = \rho(x, y, 0_-) / \rho_0, \quad (5)$$

where $\rho_0 = N_0/A$ is the surface density of N_0 incident photons distributed uniformly over the illuminated area $A = \pi w^2 / \cos \theta_0$ at the phantom surface ($z=0$).

For semi-infinite heterogeneous phantoms, we used the following parameters: $w=12.5$ mm, maximum FOV $=41.2$ mm \times 41.2 mm covered with a 201×201 grid and $d=25$ mm. To reduce the variance in the outputs of MC simulations, we averaged $\rho(x, y, 0_-)$ either along the y axis or within a region selected according to the system symmetry. We investigated the dependence of R on different combinations of optical parameters in the two regions of the phantoms to study the information content of the reflectance image data. The values of optical parameters adopted in this study are based on those of porcine skin dermis with index of refraction $n_1=n_2=1.40$ unless noted otherwise.²⁰

For validation purpose, we employed a configuration of homogeneous slab phantoms of small thickness T with the photons of incident beam uniformly distributed at the phantom surface with a direction of $(\theta_0, 0)$ in the MC code. The

TABLE I. The optical parameter values for heterogeneous phantoms.

	μ_a (mm ⁻¹)	μ_s (mm ⁻¹)	g	n
Host medium (region 1)	0.2–0.8	4.0–5.6	0.8	1.40 or 1.50
Embedded region (region 2)	0.02–2.0	3.0–8.0	0.28–0.98	1.35–1.50

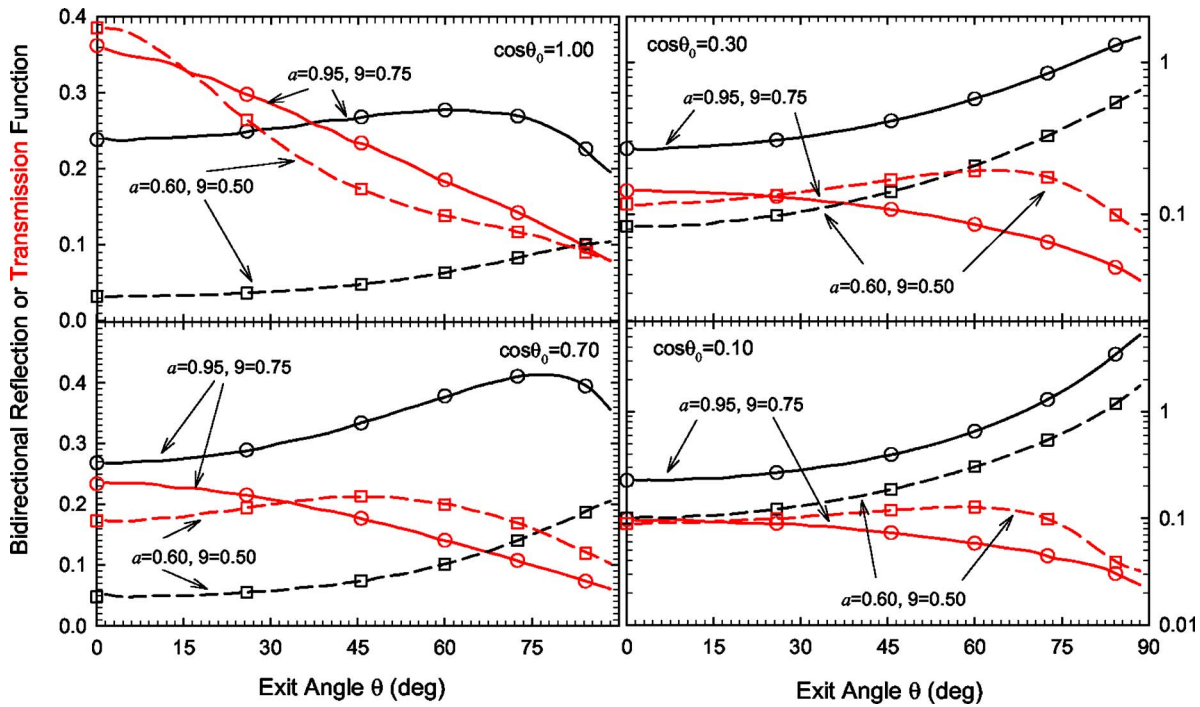


FIG. 2. The bidirectional reflection and transmission functions vs the exit angle θ for a homogeneous slab phantom of $n_1=1.00$ with $N=1.26 \times 10^7$. Two groups of phantom parameters were used (1) $a=0.95$ ($\mu_a=0.50 \text{ mm}^{-1}$, $\mu_s=9.50 \text{ mm}^{-1}$), $g=0.75$, $T=0.80 \text{ mm}$; (2) $a=0.60$ ($\mu_a=4.00 \text{ mm}^{-1}$, $\mu_s=6.00 \text{ mm}^{-1}$); $g=0.50$; $T=0.10 \text{ mm}$. The black (red) lines are the bidirectional reflection (transmission) functions calculated by the Monte Carlo method while the black (red) symbols are the corresponding values from Table 35 in Ref. 4.

reflectance $R(x, y)$ defined in Eq. (5) was converted into an angle-resolved bidirectional form of $R_b(\theta, \theta_0)$ by averaging $R(x, y)$ over the FOV, $\phi \in [0, 2\pi]$, and $\theta_i \in [(i-1/2)\Delta\theta, (i+1/2)\Delta\theta]$, with $\Delta\theta = \pi/2M$ and $i=0, 1, \dots, M$, and then multiplying the averaged R by $(\pi/\cos \theta \Delta\Omega)$, where $\Delta\Omega = 2\pi \sin \theta \Delta\theta$ is an element of the solid angle. The function $R_b(\theta, \theta_0)$ can then be compared directly to the RTE calculated values according to the bidirectional reflection function $R_b(\mu, \mu_0)$ defined in Eq. (3). Similar procedures were also used for comparison of the bidirectional transmission functions T_b .

III. RESULTS

A. Code validation and performance

The parallel MC code used for imaging simulations has been developed using the kernel of the early versions that has been tested extensively.^{11,12,19,21} We further validated this code by comparison of the bidirectional reflection and transmission functions calculated by the MC code using semi-infinite homogeneous slab phantoms with $M=30$ to those by a doubling method and compiled in the Table 35 of Ref. 4. The results for two sets of optical parameters of (μ_a, μ_s, g) and thickness T with index-matched phantoms are presented in Fig. 2. With $N_0=1.26 \times 10^7$ for each MC simulation of the reflection and transmission functions, the averaged fluctuation was found to be less than 2% based on ten different runs

(defined below). In addition, we obtained the ratio of unscattered photons in the transmitted portion of incident light to N_0 as a function of the optical thickness $\tau = \mu_t d$ which agrees well with the predicted values from the Beer-Lambert law (data not shown).

We evaluated the performance of the parallel MC code in simulating the reflectance images on a computing cluster of eight nodes (Poweredge 1750, Dell) with a total of 16 PEs (Xeon 3.06 GHz CPU, Intel) using a semi-infinite homogeneous phantom and the 201×201 surface grid. Two different sets of μ_a were used for the evaluations with $\mu_s = 6.00 \text{ mm}^{-1}$, $g=0.80$, and $n=1.50$ and the collection angle $\alpha=90^\circ$ [see Fig. 4(b) on the effect of α or NA]. The averaged fluctuation of photon numbers in a grid cell was obtained by dividing the standard deviation σ of photon numbers of the same grid cell at the surface, among ten executions of the code with identical parameters but different seeds of RNG, by their mean value m and then averaged over all grid cells within the illuminated region. The averaged fluctuation $\langle \sigma/m \rangle$ and computational time t scales with the tracked photon number N in a power relation as $\langle \sigma/m \rangle \propto N^{-0.50 \pm 0.01}$ and $t \propto N^{1.000 \pm 0.001}$. To achieve a 2% value for $\langle \sigma/m \rangle$, we found that the tracked photon number needs to be $N=1.09 \times 10^9$, and $t=313 \text{ s}$ in the case of $\mu_a=1.20 \text{ mm}^{-1}$ while $N=2.23 \times 10^8$, and $t=305 \text{ s}$ in the case of $\mu_a=0.20 \text{ mm}^{-1}$. Additionally, the test results of our parallel MC code on the 16 PE cluster show an speedup of 15.8 or an efficiency of 0.990.

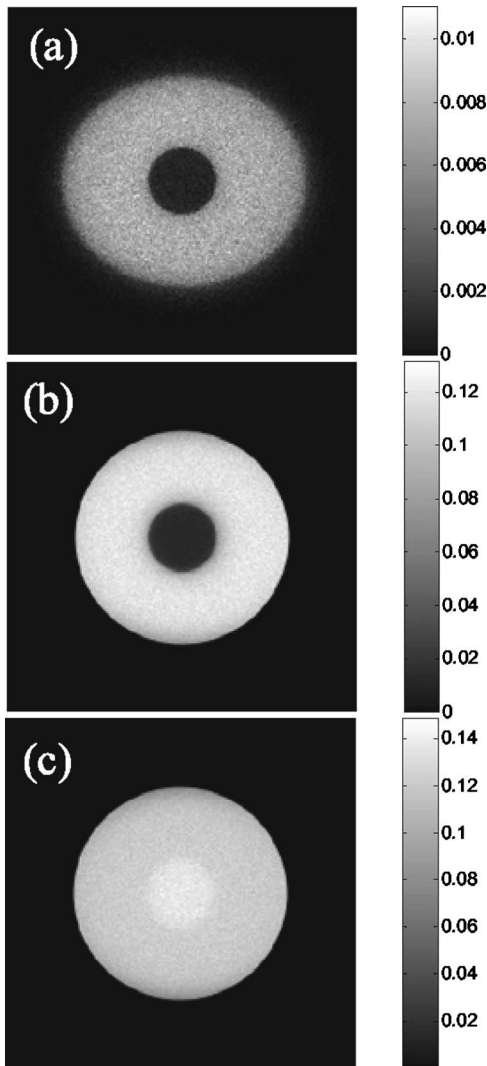


FIG. 3. Three gray-scale reflectance images $R(x, y)$ of a semi-infinite heterogeneous phantom with a 201×201 grid over an FOV of 41.2 mm along x and y axes and $\mu_{a1}=0.200 \text{ mm}^{-1}$, $\mu_{s1}=\mu_{s2}=4.00 \text{ mm}^{-1}$, $g_1=g_2=0.80$, $n_1=n_2=1.50$, and different values of μ_{a2} and collection angle α : (a) $\mu_{a2}=2.00 \text{ mm}^{-1}$, $\alpha=15.0^\circ$; (b) $\mu_{a2}=2.00 \text{ mm}^{-1}$, $\alpha=90.0^\circ$; (c) $\mu_{a2}=0.15 \text{ mm}^{-1}$, $\alpha=90.0^\circ$. Other parameters are $N_0=1.13 \times 10^8$, $w=12.5 \text{ mm}$, $\theta_0=30^\circ$, $D=0.75 \text{ mm}$, $B=8.00 \text{ mm}$.

B. Effect of numerical aperture on reflectance images

We used cylindrical shaped region 2 with different optical parameters and a surface center position at $(x_c, 0, 0)$ in the heterogeneous tissue phantoms to imitate an embedded lesion in the illuminated area. For most of the numerical results, region 2 was set to be symmetric with respect to the incident beam with $x_c=0$. Three examples of the reflectance image $R(x, y)$ are presented in Fig. 3 as observed with a camera on top of the phantoms. It should be noted that different shapes of the illuminated area between Figs. 3(a) and 3(b) is due to the effect of NA as the lens-phantom distance h decreases from 17.9 mm to 0. In Figs. 3(b) and 3(c), only the photons exiting from the phantom surface within the circular lens aperture can contribute to the images and thus make the acquired images appear circular. The images in Fig. 3 reveal two different regions in the illuminated area in

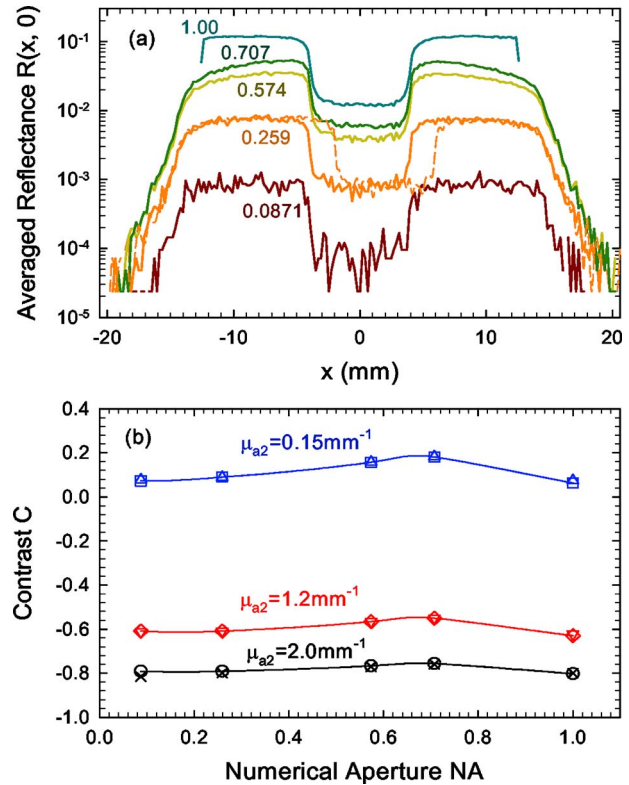


FIG. 4. (a) The x dependence of $R(x, 0)$ with $\mu_{a2}=\text{mm}^{-1}$ at different NA values as marked; the results obtained with the center of the embedded region $x_c=0$ are represented by the solid lines and the result obtained with $x_c=2.00 \text{ mm}$ is represented with a dashed line; (b) image contrast vs the numerical aperture (NA) = $\sin \theta$ for different μ_{a2} as marked with the lines as visual guides. The result obtained with $x_c=0 \text{ mm}$ are represented by symbols of $\square \diamond \circ$ and the results obtained with $x_c=2.00 \text{ mm}$ are represented by $\triangle \nabla x$. All other parameters are identical to those in Fig. 3.

which stronger light absorption in the central region leads to smaller R and vice versa. Furthermore, the R value depends not only on the optical parameters but also on the collection angle α or NA of the imaging system. These can be quantitatively analyzed by plotting the image profile $R(x, y)$ along the x axis for different NA, as shown in Fig. 4(a). Because of the symmetry, we averaged the photon density along the y axis over three rows of pixels on each side of the x axis for variance reduction. To study the effect of the symmetry of region 2, we also obtained the same set of image profiles with $x_c=2.00 \text{ mm}$ and only one off-center profile data is shown in Fig. 4(a).

From Fig. 4(a), one can see that the reflectance R increases with NA but the relative change between the two regions remains similar, indicating that the change is independent of the imaging system parameters. Based on these results, we define an image contrast C to characterize the relative change in reflectance R as

$$C = \frac{\bar{R}_c - \bar{R}_p}{\bar{R}_c + \bar{R}_p}, \tag{6}$$

where \bar{R}_c is the reflectance averaged over a circle of 6 mm diameter centered at the origin and \bar{R}_p is the reflectance av-

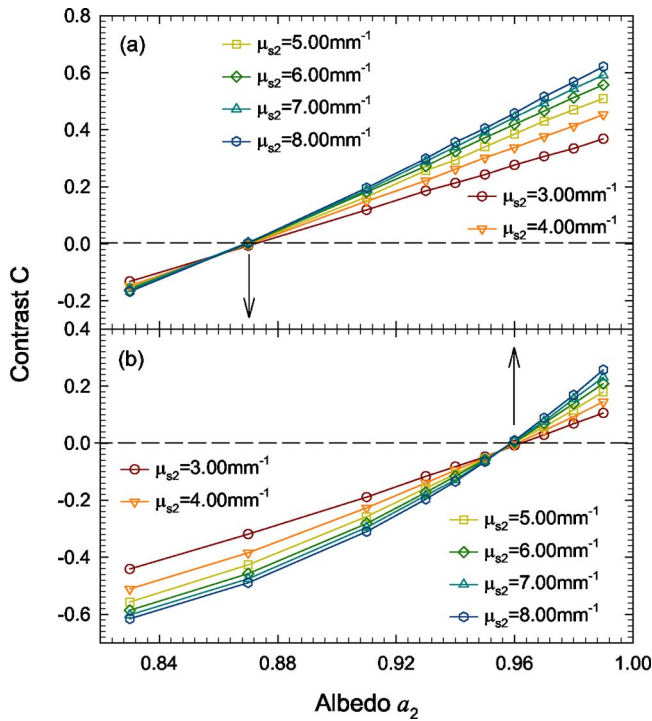


FIG. 5. The contrast vs the albedo a_2 of the central region with $D = 0.75 \text{ mm}$ for different albedo of the peripheral region: (a) $a_1 = 0.870$ and $\mu_{s1} = 6.32 \text{ mm}^{-1}$; (b) $a_1 = 0.960$ and $\mu_{s1} = 5.79 \text{ mm}^{-1}$. The scattering coefficient of the central region is marked in the figures with arrows indicating the a_1 values. The solid lines are visual guides and all other parameters are identical to those in Fig. 3.

eraged over a concentric ring in the peripheral region of illuminated area with 10 and 22 mm as the inner and outer diameters, respectively. With these definitions, we first investigated the effect of numerical aperture $\text{NA} = \sin \alpha$ of the imaging system by obtaining C as a function of NA for three different heterogeneous phantoms. The results obtained with region 2 placed at the center and off-center are presented in Fig. 4(b), which shows that C has a very weak dependence on α and is independent of the region 2 location. In fact, the relative difference between the values of C at $\text{NA} = 1.00$ and 0.087 is 0.50%, 1.8% and 4.8% for the cases of $\mu_{a2} = 0.15, 1.2, 2.0 \text{ mm}^{-1}$, respectively in Fig. 4(b). For this reason we adopted $\alpha = 90^\circ$ or $\text{NA} = 1.00$ in the following results for fast simulations with reduced variance.

C. Dependence of the image contrast on phantom parameters

MC simulations with different sets of optical parameters (μ_a, μ_s, g, n) between the two regions of heterogeneous phantoms have been carried out to find the relations between the image contrast C and phantom parameters. An analysis of these numerical image data demonstrated an interesting relation in that C depends mainly on the single-scattering albedo $a_2 = \mu_{s2} / (\mu_{a2} + \mu_{s2})$ in the central region relative to the albedo a_1 in the peripheral region when $a_1 \sim a_2$ and $g_1 = g_2$. These results are presented in Fig. 5 with the thickness of embedded region $D = 0.75 \text{ mm}$.

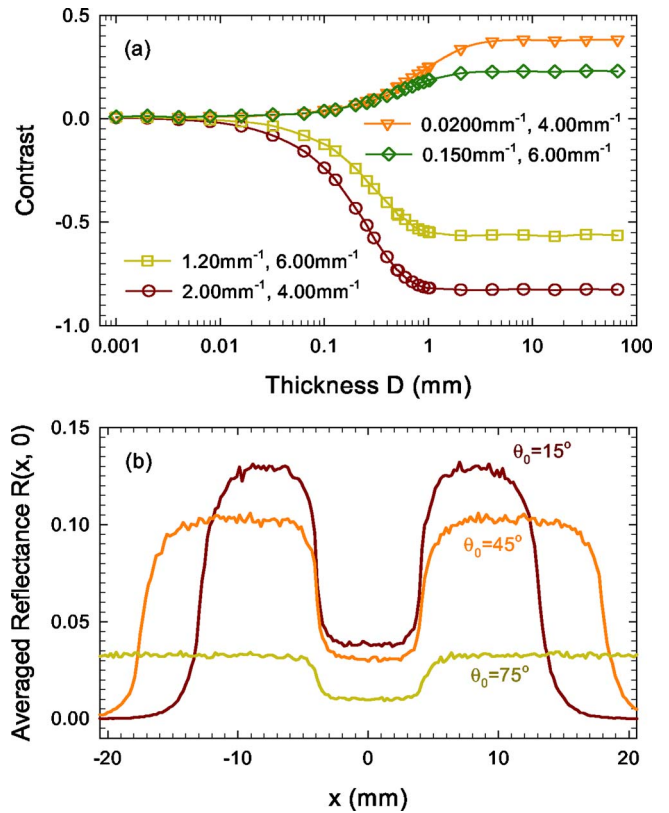


FIG. 6. (a) The contrast vs the thickness D of the central region for four sets of μ_{a2} and μ_{s2} as marked in the legends, respectively, with $g_1 = g_2 = 0.80$, $\mu_{a1} = 0.200 \text{ mm}^{-1}$, $\mu_{s1} = 4.00 \text{ mm}^{-1}$, $n_{r1} = n_{r2} = 1.40$, $\theta_0 = 30^\circ$. The lines are visual guides and all other parameters are identical to those in Fig. 3(b). The x dependence of $R(x, 0)$ at different incident angles θ_0 with $\mu_{a2} = 1.20 \text{ mm}^{-1}$, $\mu_{s2} = 6.00 \text{ mm}^{-1}$, $D = 0.75 \text{ mm}$. Other parameters are identical to those in (a).

The effects of the embedded region thickness D and incident angle θ_0 were determined on the contrast and image profiles. The contrast C is plotted in Fig. 6(a) as a function of D at a fixed value of $\theta_0 = 30^\circ$ for different sets of μ_{a2} and μ_{s2} in the embedded region. The results show that the contrast of reflectance image is sensitive to D as long as D is comparable to the photon transportation depth l_{tr} defined as $1 / [\mu_a + \mu_s(1 - g)]$. We also obtained C as a function of θ_0 at fixed values of D and found that C exhibits almost no changes with θ_0 varied from 0° to 90° . However, a close examination of the reflectance images indicated that the linear image profile $R(x, 0)$ display a strong dependence on θ_0 , as shown in Fig. 6(b). Finally, we investigated the dependence of image contrast on the anisotropy factor g_2 and refractive index n_2 of the central region in the heterogeneous phantoms and typical data are presented in Fig. 7. These results show that the image contrast C is quite sensitive to the value of g_2 of the embedded region but nearly independent of n_2 . The sensitivity of C on g_2 can be attributed to the fact that about 20% of remitted photons experience less than five-scattering events in the MC simulations and the spatial distribution of these nondiffusive photons is affected by the scattering phase function or anisotropy factor.

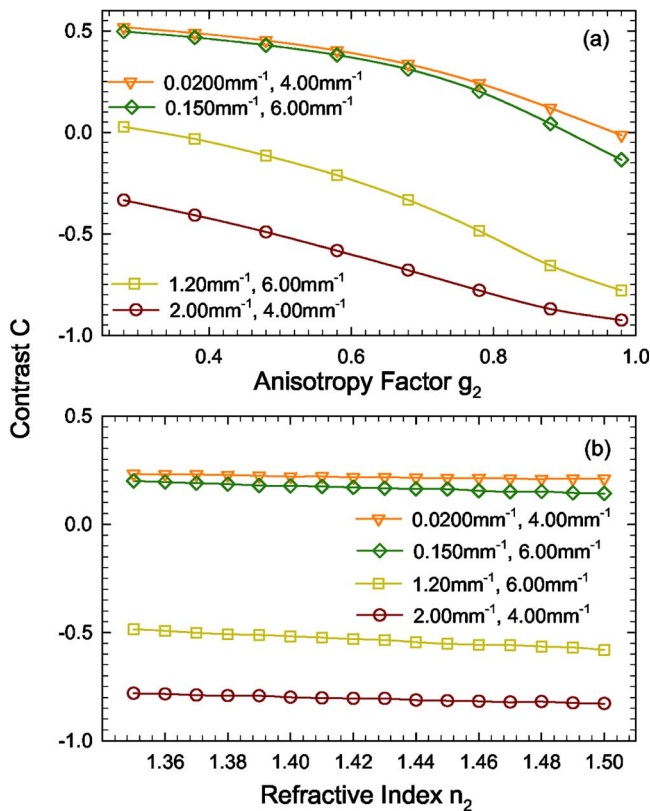


FIG. 7. The contrast vs (a) the anisotropy factor g_2 of the central region with $g_1=0.80$ and $n_1=n_2=1.40$; (b) the refractive index n_2 with $g_1=g_2=0.8$ and $n_1=1.40$ for four sets of μ_{a2} and μ_{s2} as marked in the legends, respectively. The optical parameters of the peripheral region are given by $\mu_{a1}=0.300 \text{ mm}^{-1}$, $\mu_{s1}=5.50 \text{ mm}^{-1}$. The lines are visual guides and all other parameters are identical to those in Fig. 3.

IV. DISCUSSION

The simplicity and flexibility of the MC methods have been well documented for solving various boundary-value and other problems accurately.¹⁵ In fact, the MC methods for RTE-based problems have often been used as the standard against which other methods such as the diffusion approximations are evaluated. For a long time, MC simulations have been regarded as a time-consuming method for image modeling because of the need to track large number of photons to reduce variance in the image signals with small sampling sizes. In this paper, we demonstrated that with algorithm optimization and code parallelization the MC method can generate reflectance images with a large number of pixels ($\sim 4 \times 10^4$) and negligible variance (2% or less) within minutes on a 16 PE cluster. By comparison, our test runs on a single PE of the same cluster indicated that it took about 10 hours using an existing and widely used MC code^{9,10} to generate similar reflectance images of the same variance. One should note that further improvement of MC code performance from what we described here is possible with pre-stored RNs, increase of data communication speed using the new generation of computers with 64 bit bus and larger computing clusters. As the performance-to-price ratio of computers continues to increase, one may anticipate the use of MC

method as a fast and accurate tool for forward modeling of imaging data in many types of application, including optical tomography of turbid media, over the coming years.

Several results presented in this paper on reflectance images are significant. First, we proved that the NA of the imaging system or the light collection angle α does not affect the contrast C of the reflectance images from turbid tissue phantoms even though the reflectance exhibits a sensitive dependence. Therefore, an analysis of image contrast through simulation of reflectance images can be conducted with large NA or α for reduced variance or shortened computing time. Increasing NA in the measurement of the reflected light signals could also enhance signal-to-noise ratio of the acquired images, without affecting image contrast, because the dark-current and readout noises of a typical imager are independent of NA. We have also shown in Fig. 5 that the contrast converges to 0 for the heterogeneous phantoms in which the two regions of different absorption and scattering coefficients have matched single-scattering albedos ($a_1=a_2$). This is clearly a consequence of the renormalization scheme we defined in Eqs. (1) and (2). Despite the fact that the above equations are based on geometric optics and the radiative transfer theory, their correctness remains to be checked against experimental results using heterogeneous turbid phantoms of accurately known optical parameters and carefully matched albedos. This task is currently underway in our lab.

The thickness of lesions embedded in normal tissue is, among others, an important parameter in the diagnosis and staging of dysplastic and malignant lesion in early stages. The simulation results in Fig. 6(a) show that the contrast of the reflectance images from a two-region heterogeneous phantom increase with D and reaches a saturation level when D exceeds about $3l_{tr}$ in the central region. These data demonstrated that the average penetration depth of the reflected photons from the phantom bulk is about $3l_{tr}$, and thus reflectance image signals cannot be used to determine lesion thickness when $D > 3l_{tr}$. Combined with the results displayed in Figs. 5 and 7, it is concluded that both optical and geometric parameters affect the reflectance image contrast. For most of the biological tissues in the visible and near-infrared regions, such as the skin and pigmented lesion tissues, the values of the bulk absorption and scattering coefficient ranging from 0.1 to 10 mm^{-1} and g from 0.4 to 0.9.^{2,20} This yields the values of $3l_{tr}$ to be in a range from 0.1 to 5 mm as a zone of detection for optical reflectance imaging where the existing imaging modalities are not very effective. Furthermore, this detection zone contains the superficial tissue layers where most of the dysplastic and malignant lesions begins in their early stages. We would also like to point out that the depth of the embedded lesion can be determined by acquiring reflectance images either at multiple incident angles with a single-wavelength illumination, as demonstrated by the data in Fig. 6(b), or at a single angle with multispectral images if the wavelength dependences of the optical parameters are known. An experimental investigation of reflectance imaging using tissue phantoms based on the silicone suspensions of

TiO₂ powders and pigments is currently underway. The optical parameters of the tissue phantoms are to be determined with another established method²¹ using the thin disk copies of the identical phantom materials so that the numerical results reported here can be independently verified.

It should be noted that the current MC algorithm does not account for the variation in polarization states during photon transportation. Several polarization MC algorithms have been reported, as summarized in Ref. 31. But code implementation and experimental validations are limited only to microsphere suspension based phantoms for which the Mueller matrix elements can be accurately derived from Mie theory. In contrast, biological tissues have structures much more complex than the simple two-component systems of microsphere suspensions. Therefore the modeling of photon polarization changes in tissues, including proper implementation in MC codes, is a difficult problem, which remains open to this date. Without accurate modeling, information related to polarization change will most likely remain as a means to separate the coherent reflected light due to index mismatch from the multiply scattered light emerging from the tissue bulk,³² which has been studied in this paper.

In summary, we demonstrated in this paper that the MC method can be implemented as an accurate and fast modeling tool to quantitatively model the reflectance image data acquired from biological tissues. The numerical aperture of an imaging system has been found to have little effect on the image contrast which was used to reduce variance for fast MC simulations with large collection angles. A numerical study of the reflectance images from heterogeneous tissue phantoms reveals that rich information on the structural and optical parameters of an embedded lesion can be extracted from the reflectance image data. Most importantly, it has been shown that each of the three optical parameters (μ_a, μ_s, g) correlate with the reflectance image data, which provide a solid foundation to develop a robust inverse algorithm to inversely determine those parameters by the multispectral reflectance imaging method in the near future. These results strongly suggest that the multispectral reflectance imaging method, when combined with the parallel MC method for forward calculations and an efficient inverse algorithm, has the potential to yield a noninvasive, functional and low-cost method of submillimeter resolution for the diagnosis of dysplastic and malignant lesions in the superficial tissue layers.

^{a)} Author to whom correspondence should be addressed. Electronic mail: hux@ecu.edu

¹R. R. Anderson and J. A. Parrish, "The optics of human skin," *J. Invest. Dermatol.* **77**, 13–19 (1981).

²G. Zonios, J. Bykowski, and N. Kollias, "Skin melanin, hemoglobin, and light scattering properties can be quantitatively assessed *in vivo* using diffuse reflectance spectroscopy," *J. Invest. Dermatol.* **117**, 1452–1457 (2001).

³S. L. Jacques, J. C. Ramella-Roman, and K. Lee, "Imaging skin pathology with polarized light," *J. Biomed. Opt.* **7**, 329–340 (2002).

⁴H. C. van de Hulst, *Multiple Light Scattering: Tables, Formulas, and Applications* (Academic, New York, 1980).

⁵T. J. Farrell, M. S. Patterson, and B. Wilson, "A diffusion theory model of spatially resolved, steady-state diffuse reflectance for the noninvasive determination of tissue optical properties *in vivo*," *Med. Phys.* **19**, 879–888 (1992).

⁶S. A. Carp, S. A. Prahl, and V. Venugopalan, "Radiative transport in the delta-P1 approximation: accuracy of fluence rate and optical penetration depth predictions in turbid semi-infinite media," *J. Biomed. Opt.* **9**, 632–647 (2004).

⁷H. Jiang, Y. Xu, and N. Iftimia, "Experimental three-dimensional optical image reconstruction of heterogeneous turbid media from continuous-wave data," *Opt. Express* **7**, 204–209 (2000).

⁸B. C. Wilson and G. Adam, "A Monte Carlo model for the absorption and flux distributions of light in tissue," *Med. Phys.* **10**, 824–830 (1983).

⁹S. A. Prahl, M. Keijzer, S. L. Jacques, and A. J. Welch, "A Monte Carlo Model of Light Propagation in Tissue," SPIE Institute Series **5**, 102–111 (1989).

¹⁰L. Wang, S. L. Jacques, and L. Zheng, "MCML-Monte Carlo modeling of light transport in multi-layered tissues," *Comput. Methods Programs Biomed.* **47**, 131–146 (1995).

¹¹Z. Song, K. Dong, X. H. Hu, and J. Q. Lu, "Monte Carlo simulation of converging laser beams propagating in biological materials," *Appl. Opt.* **38**, 2944–2949 (1999).

¹²J. Q. Lu, X. H. Hu, and K. Dong, "Modeling of the rough-interface effect on a converging light beam propagating in a skin tissue phantom," *Appl. Opt.* **39**, 5890–5897 (2000).

¹³P. K. Yalavarthy, K. Karlekar, H. S. Patel, R. M. Vasu, M. Pramanik, P. C. Mathias, B. Jain, and P. K. Gupta, "Experimental investigation of perturbation Monte-Carlo based derivative estimation for imaging low-scattering tissue," *Opt. Express* **13**, 985–997 (2005).

¹⁴K. Mosegaard and M. Sambridge, "Monte Carlo analysis of inverse problems," *Inverse Probl.* **18**, R29–R54 (2002).

¹⁵G. S. Fishman, *Monte Carlo: Concepts, Algorithms, and Applications* (Springer-Verlag, New York, 1996).

¹⁶K. Li, J. Q. Lu, R. S. Brock, B. Yang, and X. H. Hu, "Quantitative modeling of skin images using parallel Monte Carlo methods," *Proc. SPIE* **5693**, 82–87 (2005).

¹⁷N. Joshi, C. Donner, and H. W. Jensen, "Noninvasive measurement of scattering anisotropy in turbid materials by nonnormal incident illumination," *Opt. Lett.* **31**, 936–938 (2006).

¹⁸Y. Du, X. H. Hu, M. Cariveau, X. Ma, G. W. Kalmus, and J. Q. Lu, "Optical properties of porcine skin dermis between 900 nm and 1500 nm," *Phys. Med. Biol.* **46**, 167–181 (2001).

¹⁹X. Ma, J. Q. Lu, R. S. Brock, K. M. Jacobs, P. Yang, and X. H. Hu, "Determination of complex refractive index of polystyrene microspheres from 370 to 1610 nm," *Phys. Med. Biol.* **48**, 4165–4172 (2003).

²⁰X. Ma, J. Q. Lu, H. Ding, and X. H. Hu, "Bulk optical parameters of porcine skin dermis tissues at eight wavelengths from 325 to 1557 nm," *Opt. Lett.* **30**, 412–414 (2005).

²¹C. Chen, J. Q. Lu, H. Ding, K. M. Jacobs, Y. Du, and X. H. Hu, "A primary method for determination of optical parameters of turbid samples and application to intralipid between 550 and 1630 nm," *Opt. Express* **14**, 7420–7435 (2006).

²²Max Born and Emil Wolf, *Principles of Optics: Electromagnetic Theory of Propagation, Interference and Diffraction of Light*, 7th (expanded) ed. (Cambridge University Press, Cambridge, England; New York, 1999).

²³J. M. Tualle and E. Tinet, "Derivation of the radiative transfer equation for scattering media with a spatially varying refractive index," *Opt. Commun.* **228**, 33–38 (2003).

²⁴W. H. Press, B. P. Flannery, S. A. Teukolsky, and W. T. Vetterling, *Numerical Recipes in Fortran 77—The Art of Scientific Computing*, 2nd ed. (Cambridge University Press, New York, 1992).

²⁵O. E. Percus and M. H. Kalos, "Random Number generators for MIMD parallel processors," *J. Parallel Distrib. Comput.* **6**, 477–497 (1990).

²⁶Scalable Parallel Random Number Generators (SPRNG) test suite, <http://www.nersc.gov/nusers/resources/software/libs/math/random/www/index.html>.

²⁷J. Q. Lu, Y. Feng, R. E. Cuenca, Y. Ti, K. Li, K. M. Jacobs, S. B. Jackson, R. R. Allison, C. H. Sibata, G. H. Downie, and X. H. Hu, "Multivariate analysis of Monte Carlo generated images for diagnosis of dysplastic lesions," *Proc. SPIE* **5692**, 29–36 (2005).

²⁸H. Ding, J. Q. Lu, W. A. Wooden, P. J. Kragel, and X. H. Hu, "Refractive indices of human skin tissues at eight wavelengths and estimated dispersion relations between 300 and 1600 nm," *Phys. Med. Biol.* **51**,

- 1479–1489 (2006).
- ²⁹X. H. Hu, W. A. Wooden, S. J. Vore, M. J. Cariveau, Q. Fang, and G. W. Kalmus, “*In vivo* study of intradermal focusing for tattoo removal,” *Lasers Med. Sci.* **17**, 154–64 (2002).
- ³⁰H. Ding, J. Q. Lu, K. M. Jacobs, and X. H. Hu, “Determination of refractive indices of porcine skin tissues and intralipid at eight wavelengths between 325 and 1557 nm,” *J. Opt. Soc. Am. A* **22**, 1151–1157 (2005).
- ³¹J. C. Ramella-Roman, S. A. Prahl, and S. L. Jacques, “Three Monte Carlo programs of polarized light transport into scattering media: part I,” *Opt. Express* **13**, 4420–4438 (2005).
- ³²S. P. Morgan and I. M. Stockford, “Surface-reflection elimination in polarization imaging of superficial tissue,” *Opt. Lett.* **28**, 114–116 (2003).